scientific reports

Check for updates

OPEN

Stabilization and electronic topological transition of hydrogen-rich metal Li_5MoH_{11} under high pressures from first-principles predictions

Prutthipong Tsuppayakorn-aek[1,2], Wiwittawin Sukmas[1,2], Rajeev Ahuja[3,4], Wei Luo[3] & Thiti Bovornratanaraks[1,2]✉

Regarded as doped binary hydrides, ternary hydrides have recently become the subject of investigation since they are deemed to be metallic under pressure and possibly potentially high-temperature superconductors. Herein, the candidate structure of Li_5MoH_{11} is predicted by exploiting the evolutionary searching. Its high-pressure phase adopts a hexagonal structure with $P6_3/mcm$ space group. We used first-principles calculations including the zero-point energy to investigate the structures up to 200 GPa and found that the $P6_3cm$ structure transforms into the $P6_3/mcm$ structure at 48 GPa. Phonon calculations confirm that the $P6_3/mcm$ structure is dynamically stable. Its stability is mainly attributed to the isostructural second-order phase transition. Our calculations reveal the electronic topological transition displaying an isostructural second-order phase transition at 160 GPa as well as the topology of its Fermi surfaces. We used the projected crystal orbital Hamilton population (pCOHP) to examine the nature of the chemical bonding and demonstrated that the results obtained from the pCOHP calculation are associated with the electronic band structure and electronic localized function.

The success of experimental syntheses of metal hydrides has attracted considerable attention especially amongst the high-pressure research community, a corollary to discoveries—both experimental and theoretical—of a variety of interesting physical properties of these materials[1–8]. Also, metal hydrides have long been considered as one of the best candidates for high-temperature superconductors. The superhydride Ce-H system, for instance, was successfully synthesized using the laser-heated diamond anvil cell (DAC) accompanied with synchrotron X-ray diffraction, which was theoretically confirmed by the evolutionary variable-composition simulation indicating that CeH_9 adopts a hexagonal clathrate structure with the $P6_3/mmc$ symmetry and potentially produces high-temperature superconductivity with estimated T_c of 105–117 K at 200 GPa[9]. Another metal-hydride superconductor of LaH_{10} with T_c = 260 K, approaching room temperature, was synthesized and experimentally observed under pressure between 180–200 GPa[10], while it was suggested by a subsequent theoretical study to adopt a sodalite-like clathrate structure with $Fm\bar{3}m$ symmetry and exhibit a decreasing trend in T_c under an increase of pressure[11]. Additionally, LaH_{11} is expected to produce high T_c as theoretically predicted[12] as well as several other materials[13–19].

More recently, ternary superhydrides (compounds each consisting of two substituted metal elements and hydrogen atoms) have been proposed to achieve metallicity and that one can expect a near room-temperature superconductivity out of them[10,11,17,18]. However, the ternary hydride Li_5MoH_{11} does not at all exhibit high-temperature superconductivity under high pressure, only with its maximum T_c of 6.5 K at 160 GPa belonging to the high-pressure phase[20]. Li_5MoH_{11} being one of the family of the hydrogen-rich metals Li_5MH_{11}, where M

[1]Extreme Conditions Physics Research Laboratory (ECPRL) and Physics of Energy Materials Research Unit, Department of Physics, Faculty of Science, Chulalongkorn University, Bangkok 10330, Thailand. [2]Thailand Centre of Excellence in Physics, Ministry of Higher Education, Science, Research and Innovation, 328 Si Ayutthaya Road, Bangkok 10400, Thailand. [3]Condensed Matter Theory Group, Department of Physics and Materials Science, Uppsala University, Box 530, 751 21 Uppsala, Sweden. [4]Applied Materials Physics, Department of Materials and Engineering, Royal Institute of Technology (KTH), 100 44 Stockholm, Sweden. ✉email: thiti.b@chula.ac.th

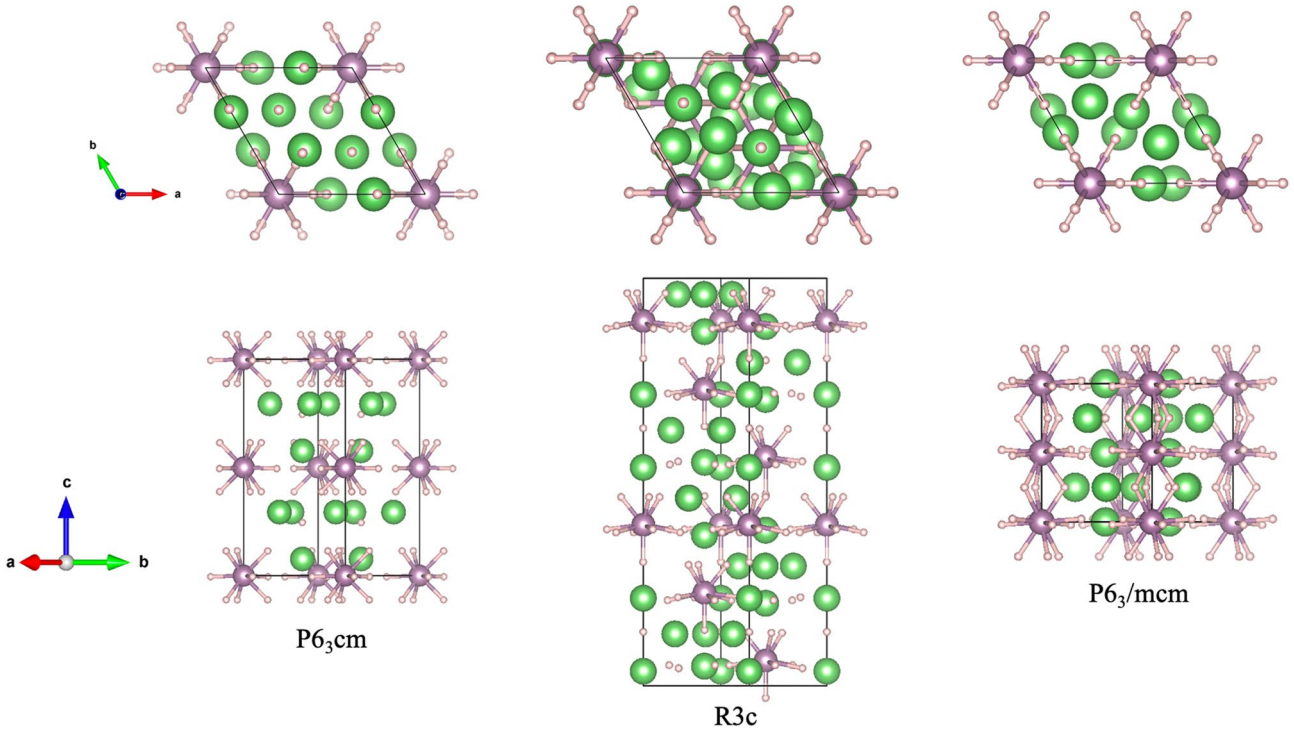

Figure 1. The crystal structures of Li_5MoH_{11}. The green, purple, and pink spheres represent, respectively, Li, Mo, and H atoms. (drawn by VESTA (ver. 3.4.7)[65] (URL https://jp-minerals.org/vesta/en/download.html)).

= Mo, W, Nb, and Ta[21], adopts a hexagonal structure with the $P6_3cm$ space group at ambient pressure, which is constructed via the ionic bonds of *i.e.* Li^+, H^-, and the ninefold-hydrogen-coordinated $[MoH_9]^{3-}$. The structure was also predicted in theory to exhibit an insulator–metal transition under compression[21]. As for Li_5MoH_{11}, it was revealed that the $P6_3cm$ structure transforms into the *Cc* and *Pc* structures at 5 GPa and 94 GPa, respectively[21]. Not long ago an experimental study utilizing high-pressure synchrotron x-ray diffraction (XRD) cast doubt on the ambiguity in structural determination of this ternary compound. According to the observation, the *Cc* and *Pc* structures do not exist at the predicted pressures (5 GPa and 94 GPa, respectively) as well as the fact that at higher pressure the crystal structure of Li_5MoH_{11} cannot also be determined experimentally[20].

In this work, we aimed to identify the unknown structure of Li_5MoH_{11} above 160 GPa, taking the crystal structure obtained from experiment as the starting structure throughout the entire calculation, by using the Universal Structure Predictor: Evolutionary Xtallography (USPEX). It is well-known that the standard spin-polarized DFT calculation, specifically within the generalized gradient approximation (GGA functional), cannot successfully describe the *d*-orbital of a transition metal[22], e.g. Mo atom[23], due highly to the strongly correlated orbitals. In order to fully take into account the valence states of Mo atom, we performed the GGA+U calculations with the objective of correctly determining the reliable values of U_{eff} for Li_5MoH_{11}. Regarding its potential for superconductivity, the electronic structure and the nature of the chemical bonding observed by the experimental study[20] were shown to propound a possibility of T_c. Again, the aforementioned experimental observation found that Li_5MoH_{11} has two different superconducting phases, indicating that a phase transition at 160 GPa might be expected to be an isostructural second-order phase transition, while the possibility of which is supported by means of an electronic topological transition (ETT). The concept of ETT has successfully been used to describe the nature of the electronic structures in several materials[24–28], particularly the metal hydride class[24]. It was also shown that ETT plays a crucial role in electronic band structure via the association with the topology of the Fermi surface (FST)[29,30]. In effect, the relationship between ETT and FST provides new insight into the nature of the electronic structure of Li_5MoH_{11}, as will be discussed later. We also support results of electronic band structure and electron localized function by demonstrating the projected crystal orbital Hamilton population (pCOHP) method.

Results and discussion

We used USPEX to predict the crystal structure of the hydrogen-rich metal Li_5MoH_{11} under high pressure and found that there exist two low-enthalpy structures adopting structurally identical hexagonal structures with *R3c* and $P6_3/mcm$ space groups. The predicted structures are shown in Fig. 1, while the optimized structural parameters for the *R3c* and the $P6_3/mcm$ structures are presented in Table 1. Subsequently the calculated structural parameters have been fitted to the Birch-Murnaghan equation of state (EOS), as summarized in Table 2. We initially conjectured that Mo^- might accept electrons from the surrounding Li^+ cations under pressure[23]. Also, Mo atom is reported to have an unusual spin-coupling that eventually modifies the oxidation state[31]. We thus applied the GGA and GGA+U_{eff} methods to investigate the possibility of this effect. In both cases, Mo^- was

Space group	Pressure (GPa)	Lattice parameters Å, °)	Atomic coordinates (fractional)
R3c	60	a = 5.104 b = 5.104 c = 18.990	Li1 (0.989, 0.564, 0.960)
		$\alpha = 90\ \beta = 90\ \gamma = 120$	Li2 (0, 0, 0.714)
			Li3 (0.667, 0.333, 0.869)
			Mo1 (0, 0, 0.895)
			H1 (0.317, 0.987, 0.709)
			H2 (0.876, 0.540, 0.796)
			H3 (0.345, 0.002, 0.883)
			H4 (0, 0, 0.803)
			H5 (0.333, 0.667, 0.798)
$P6_3/mcm$	160	a = 4.644 b = 4.644 c = 5.638	Li1 (0.667, 0.333, 1)
		$\alpha = 90\ \beta = 90\ \gamma = 120$	L2 (1, 0.587, 0.750)
			Mo1 (0, 0, 1)
			H1 (1, 0.221, 0.750)
			H2 (0.634, 0, 1.024)
			H3 (0.333, 0.667, 0.75)

Table 1. Structures of Li_5MoH_{11}.

Space group	V_0 (Å^3)	B_0 (GPa)	Method
$P6_3cm$	151.1	21.9	Without ZPE
$P6_3cm$	133.9	42.4	ZPE
R3c	144.3	21.8	Without ZPE
R3c	166.5	10.5	ZPE
$P6_3/mcm$	109.7	51.5	Without ZPE
$P6_3/mcm$	97.3	114.8	ZPE

Table 2. The structural parameters calculated by the Birch–Murnaghan equation of state.

found to not accept any electron from the surrounding Li^+ cations due to the fact that the predicted structure of Li_5MoH_{11} structure is verified as being nonmagnetic (NM), since its magnetization is equal to zero. The selected value of U_{eff} plays a decisive role in structural stability as well[32–35]. In the case of Li_5MoH_{11}, we thus evaluated the corresponding structural phase transition and electronic properties without incorporating U_{eff}.

The structural phase transitions of Li_5MoH_{11} are presented by the relative enthalpy, which is obtained from the difference between the enthalpy calculated and that of the $P6_3cm$ structure, as a function of pressure. According to our calculations, the $P6_3cm$ structure transforms into the *R*3*c* structure at 48 GPa, followed by the existence of the $P6_3/mcm$ structure at 64 GPa, as shown in Fig. 2a. Addition to this, the corresponding structural stability is further confirmed by the incorporation of the zero-point energy (ZPE) of the nuclei estimation, indicating that the *R*3*c* structure is not energetically favored at all throughout the whole pressure range, as shown in Fig. 2b. Rather, the $P6_3cm$ crystal only transitions into the $P6_3/mcm$ structure at 48 GPa, which was previously pointed out that the *R*3*c* structure becomes unstable when taking into account the effect of ZPE[36–38]. The $P6_3/mcm$ structure, therefore, is thermodynamically stable over a wide range of pressures. When it comes to dynamical stability, the harmonic approximation incorporating ZPE of nuclei scheme is used to investigate the nature of the lattice dynamics of Li_5MoH_{11}. Reported in Fig. 3a, the phonon dispersions accounting for $P6_3cm$ structure at 40 GPa was computed and the structure is demonstrated to be stable, whereas upon a compression up to 50 GPa this symmetry is dynamically unstable due to the presence of negative frequency branches, as evidenced in Fig. 3b. In effect, the $P6_3cm$ structure has a tendency to transform into the $P6_3/mcm$ structure at this very pressure. The inclusion of ZPE calculation apparently plays a crucial role in determining the stable structure of Li_5MoH_{11} under pressure, as previously demonstrated in other metal hydride systems[39,40]. Regarding the *R*3*c* phase, the responsible pressure-dependent phonon dispersion displays a tiny soft-mode at the Γ-point which is shown in Fig. 3c, accompanied by a zoomed-in $K - \Gamma - M$ path in Fig.3d. This suggests a possibility of becoming a meta-stable structure for the *R*3*c* phase, while the really stable phase belongs to the $P6_3/mcm$ structure.

Upon a series of compression, the $P6_3/mcm$ structure is clearly confirmed to be dynamically stable by the absence of negative frequency in the phonon spectra, as can be seen in Fig. 4, which implies that the compression promoted the global minimum enthalpy of the structure. At this point, we found that the $P6_3/mcm$ structure is dynamically favored over the $P6_3cm$ and *R*3*c* structures under a wide range of pressure, i.e., beginning at 80 GPa. According to the phonon density of states responsible for both Li and H atoms at around 25 THz (Fig. 4b–d), it is obvious that there exists coupling phonon branches, while they each tend to separate and eventually result in the intermediate optical phonon modes. It is worth noting that there remains the plausibility for Li_5MoH_{11} to have a phase transition due to the fact that it was previously observed to superconduct with two different

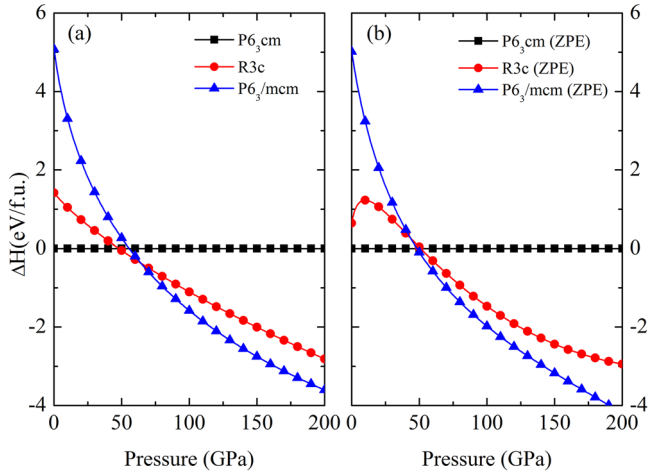

Figure 2. (a) The relative enthalpy as a function of pressure of Li_5MoH_{11} without ZPE and (b) the relative enthalpy as a function of pressure of Li_5MoH_{11} with ZPE.

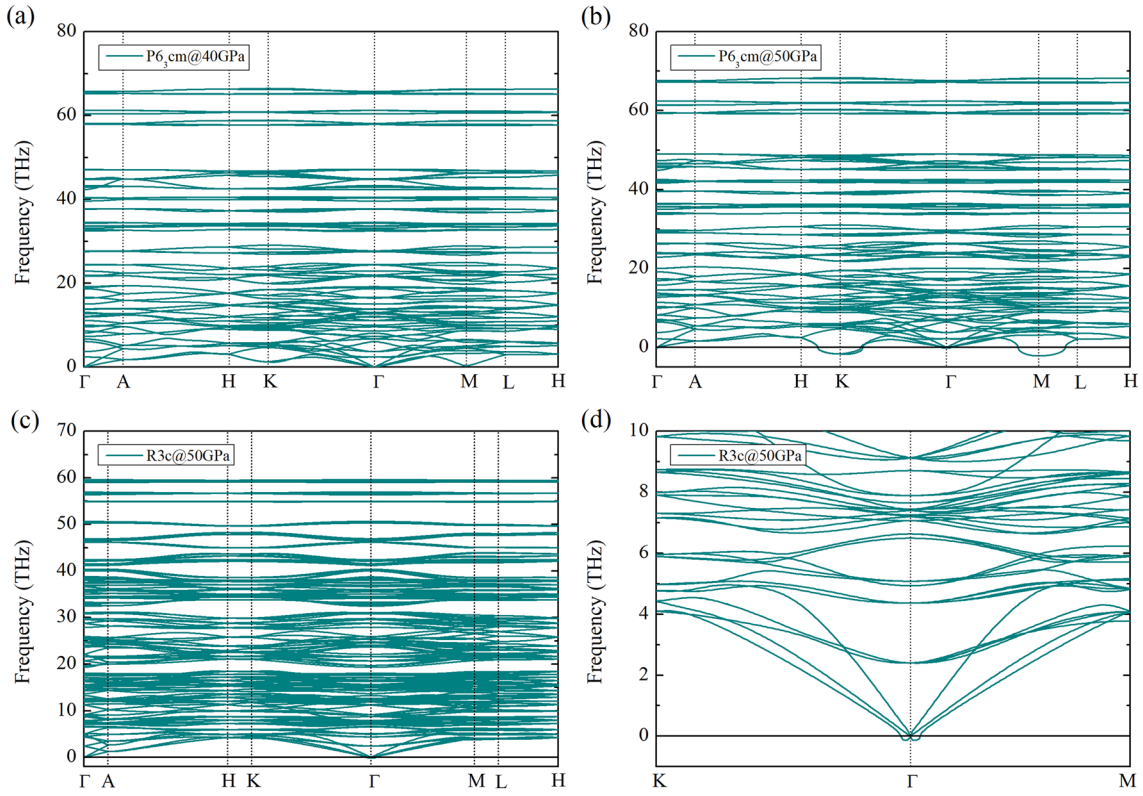

Figure 3. The phonon dispersion of Li_5MoH_{11} (a) $P6_3$/cm at 40 GPa. (b) $P6_3$/cm at 50 GPa (c) *R3c* at 50 GPa (d) soft-mode at the Γ–point of *R3c* at 50 GPa.

superconducting phases at 160 GPa[20]. At this point, however, it is difficult to verify whether there exists another phase of Li_5MoH_{11} aside from the $P6_3$/mcm structure, which, as a consequence, is expected to undergo the iso-structural second-order phase transition above 160 GPa, as previously pointed out by means of the appearance of the intermediate optical phonon modes[41] .

The electronic band structures of the $P6_3$/mcm Li_5MoH_{11} under varying pressures are plotted in Fig. 5a–d. The Mo atom's 4d orbitals split into two energy levels, i.e, E_{2g} (d_{xy}, $d_{x^2-y^2}$) and E_{1g} (d_{yz}, d_{xz}), whereas the Li atom's 2p orbitals yield the E_{1u} (p_x, p_y) and the A_{2u} (p_z) orbitals as well as into the A_{1g} orbital arising from the H atom's 1s orbital. The band structure evidences a coupling between the E_{2g} of Mo atom and the E_{1u} orbitals of Li atom and reveals a Dirac-like cone, as also found recently[42,43], at the Γ-point in Fig. 5a, which is originated from the coupling between the δ- and π-bonds. Upon an increase of pressure, particularly at 100 GPa (see Fig. 5b), the

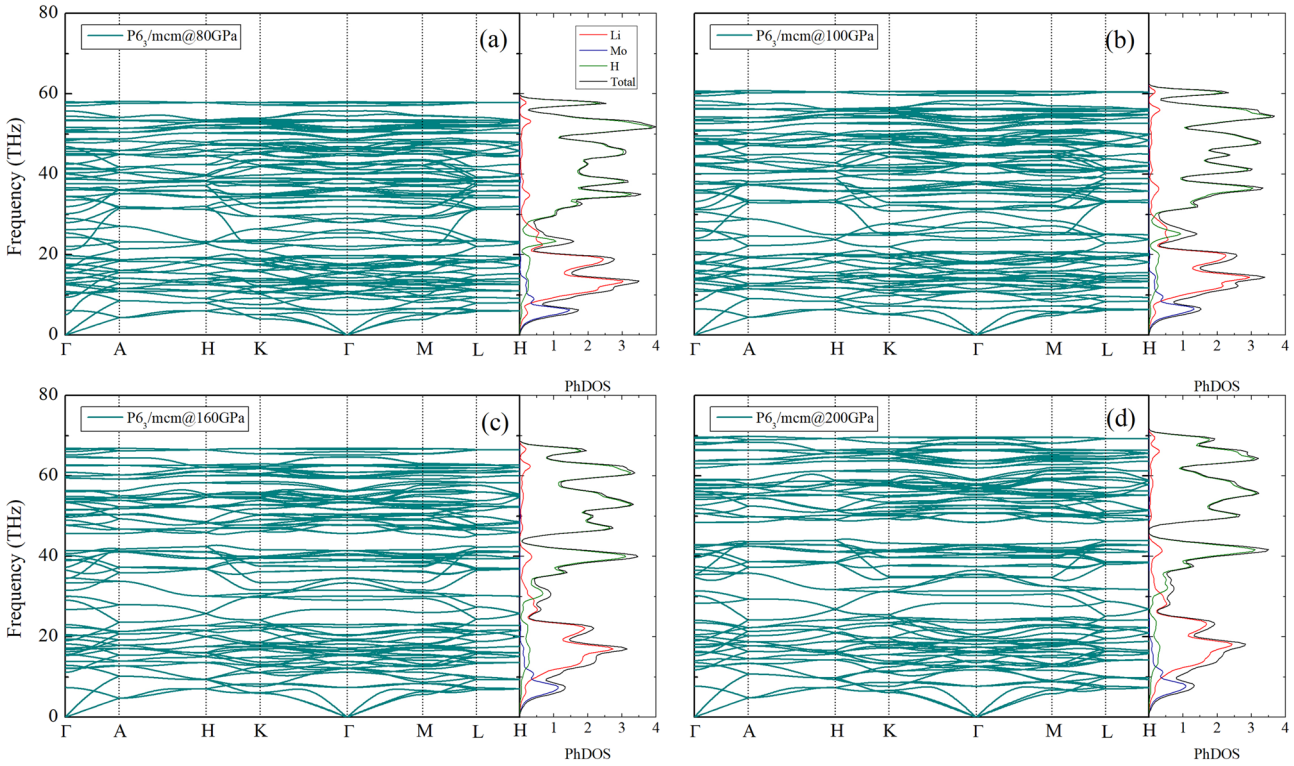

Figure 4. The phonon dispersion of Li_5MoH_{11} (a) $P6_3/mcm$ at 80 GPa, (b) $P6_3/mcm$ at 100 GPa, (c) $P6_3/mcm$ at 160 GPa, and (d) $P6_3/mcm$ at 200 GPa, respectively.

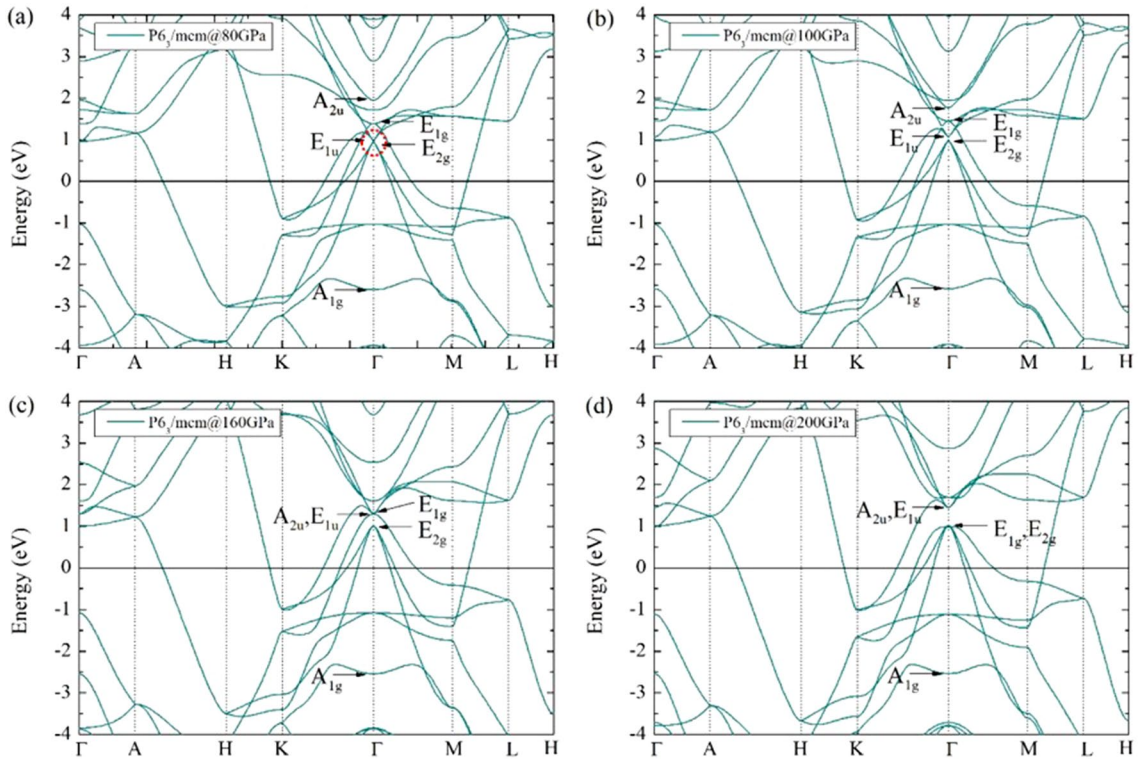

Figure 5. The band structure of Li_5MoH_{11} (a) $P6_3/mcm$ at 80 GPa, (b) $P6_3/mcm$ at 100 GPa, (c) $P6_3/mcm$ at 160 GPa, and (d) $P6_3/mcm$ at 200 GPa, respectively.

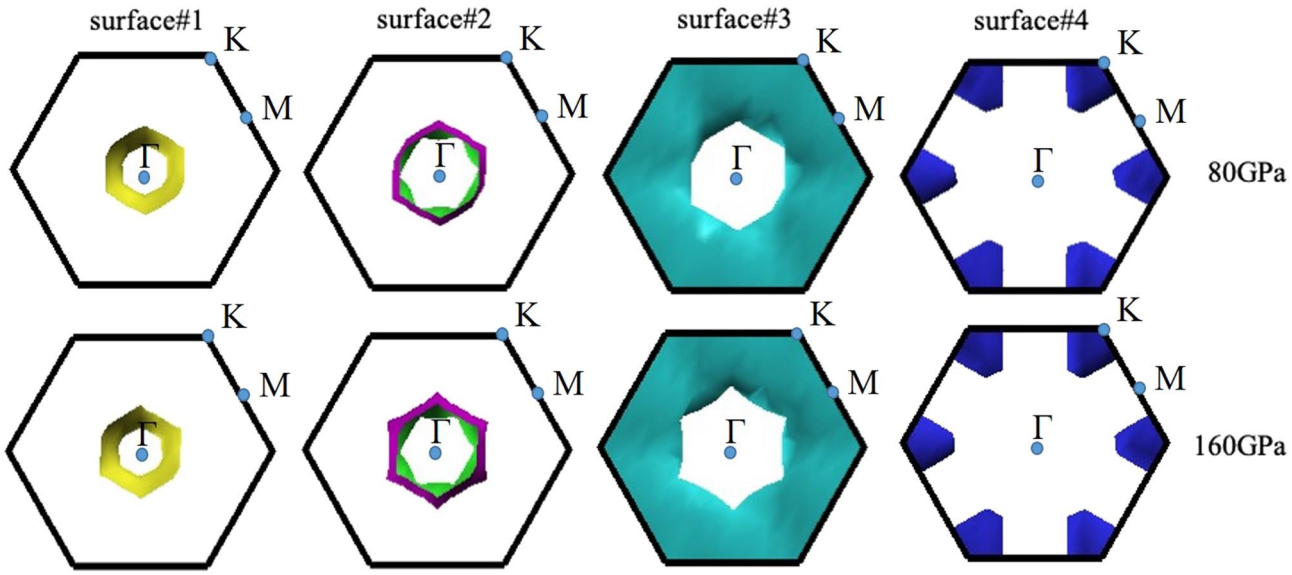

Figure 6. Sketch of FST of $P6_3/mcm$ at 80 and160 GPa, respectively (drawn by XCrySDen program (ver. 1.5.60)[66] (URL http://www.xcrysden.org/Download.html#_toc_1)).

separation of the E_{2g} orbitals of Mo and the E_{1u} orbitals of Li become apparent. This implies the electronic topological transition, which is referred to as the Lifshitz transition[44]. The following dispersion (see Fig. 5c) displays a downward shift of the A_{2u} orbitals of Li, which in turn leads to the coupling between the E_{1u} orbital of Li and the E_{1g} orbital of Mo that exhibit the σ–π bonding, at 160 GPa, when eventually the latter is roughly level with the E_{2g} orbitals of Mo atom at 200 GPa also exhibiting σ–δ bonding. Likewise, the A_{2u} orbitals of Li continue to couple with the E_{1u} orbitals of Li despite the increase of pressure, which results in σ–π bonding. As mentioned earlier, isostructural second-order phase transition induced by the $P6_3/mcm$ structure can be made possible by the Lifshitz transition. Moreover, the electronic band structures show no sign of flat bands near the Fermi level. Even though a set of flat bands can be spotted near the Fermi level as well as the presence of van Hove singularities (vHs) within H_3S[13], YH_6 and YH_{10}[14] systems, leading to the possibility of achieving high values of T_c, this can be alternatively explained by the shape of the electronic band structure or density of states of our system. Our system's electronic structures are similar to those found in YSH_6[15], $LaSH_6$[15], CeH_9[16], and CeH_{10}[19], in terms of steep branches near the Fermi level. However, we found that Li_5MoH_{11} does not exhibit high-temperature superconductivity. As an explanation, the energy level of the H atom (the A_{1g} orbitals) is lower than the Fermi level by -2.605 to -2.538 eV at 80 to 200 GPa, respectively, which further supports the implication that the high-pressure phase observed by experiment does not give high-temperature superconductivity[20].

Another key finding that needs to be mentioned is the Fermi surface topology (FST). It is well-known that the FST is associated with an electronic topological transition (ETT), which originates from a given electronic band structure[24–28], that plays a key role in promoting the second-order phase transition[45]. This was previously emphasized in previous studies[29,30] the change of material's topology is promoted by a compression. As depicted in Fig. 6, the characteristics of the FST clearly increase the likelihood of isostructural second-order phase transition: there are individual variations in surface#2 and surface#3 at 160 GPa , compared to those at 80 GPa. The topological changes in FST corresponds to the electronic band structures calculated. Thus the isostructural second-order phase transition of Li_5MoH_{11} can be described by the presence of ETT. More interestingly, surface#2 and surface#3 both form the Fermi surface nesting at the pockets surrounding the Γ-point at 160 GPa, holding a vital clue to superconductivity[29].

The likelihood of finding an electron in the neighborhood space of Li_5MoH_{11} can be measured by the electron localization function (ELF)[46], as reported in Fig. 7a. The tendency of electron localization in the $P6_3/mcm$ structure is described by uniform electron gas of the same density[19,47–50]. The calculated ELF reveals a set of chemical bonding at 0 GPa. The distances between the first (Li–Mo), second (Li–H), third (Mo–H), and fourth (H–H) nearest neighbors (NN) read 2.94826 Å, 1.83412 Å, 1.90874 Å, and 2.24193 Å, respectively. There exists electronic probability weakly accumulating between the first NN Li–Mo, the second NN Li–H, and the third NN Mo–H, particularly the bonding between the fourth NN H–H which indicates that it is likely to be a strong bonding at 0 GPa. Upon further compression up to 160 GPa, the ELF displays that the distance between the first NN Li–Mo, second NN Li–H, third NN Mo–H, and fourth NN H–H are 2.38216 Å, 1.55862 Å, 1.70037 Å, and 1.27095 Å, respectively. It is worth noting that there is also a strong bonding between H and H, and the increase of electronic distribution between Mo and H at 0 GPa, implying that H–H bonding is likely to be a strong covalent bonding. We further investigated the nature of the chemical bonding near the Fermi level by with the aid of the projected crystal orbital Hamilton populations (pCOHP) calculation, which enables the determination of anti-bonding and bonding characteristics, e.g., covalent bonds, along energy range[51–53]. Illustrated in Fig. 7b, it is obvious that the projected wave function of the Li–Mo bonding displays anti-bonding, in a good agreement with ELF and corresponds to anti-bonding in the electronic band structure[54]. Our calculations also reveal that the E_{1u} orbitals

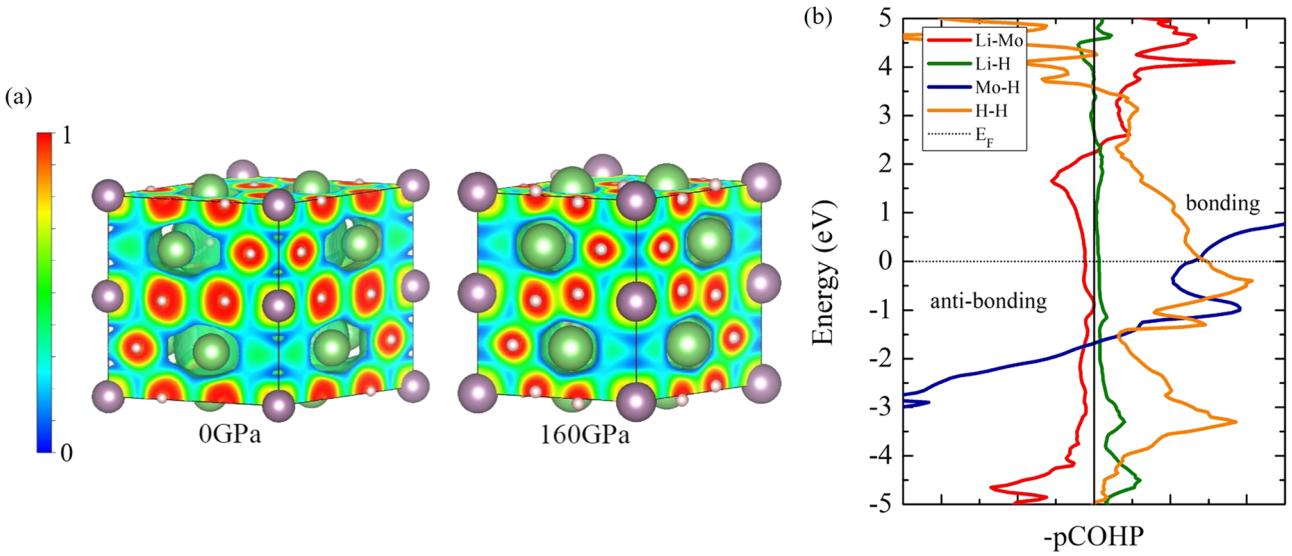

Figure 7. (a) The 3D-electron localization function (ELF) in Li_5MoH_{11} structure at 0 and 160 GPa, respectively. (drawn by VESTA (ver. 3.4.7)[65] (URL https://jp-minerals.org/vesta/en/download.html)) (b) Projected crystal orbital Hamilton populations (pCOHPs) in Li_5MoH_{11} structure at 160 GPa.

and the E_{1g} orbitals exhibit the σ–π bonding, by a determination of the electronic band structure. The projected wave function of the Li–H bonding is proved to be an ionic bond, which is confirmed by the ELF calculation, while those of the Mo–H and H–H bondings are indicated to be covalent bonds. In particular, the ELF calculation remarkably suggests a a strong covalent bond as a result of the H–H bonding. So, the characteristic of the Li–Mo anti-bonding implies that Li_5MoH_{11} cannot achieve a high value of T_c.

Conclusion

In this work, we identify the high-pressure phases of Li_5MoH_{11} by performing an evolutionary searching. Our calculations show that by incorporating the zero-point energy evaluation the $P6_3/mcm$ structure is thermodynamically and dynamically favored over the $P6_3cm$ and *R3c* structures above 50 GPa The perspective of theoretical inspection points out that the $P6_3mcm$ structure exists under high pressure adopting the hexagonal basis. Phonon dispersion calculations and the electronic topological transition reveal that the $P6_3/mcm$ structure exhibits an isostructural second-order phase transition. Also, we have shown that the topology of the Fermi surface is associated with the electronic band structure, which nonetheless does not exhibit any flat bands near the Fermi level. This reflects that fact that Li_5MoH_{11} does not have a high value of T_c. Here, our calculations support the experimental observations of T_c in the previous study[20]. The nature of the chemical bonding is associated with the electronic band structure, implying that the characteristics of the chemical bonding entail the value of T_c.

Methods

The searching for the structures of the hydrogen-rich metal Li_5MoH_{11} was performed by USPEX[55]. In all subsequent generations, the random symmetric algorithm employed 40% heredity, 20% random symmetric, 20% soft mutation, and 20% transmutation operators in the pressure range from 160 to 200 GPa with structures containing up to four formula units. All structures were fully relaxed using the generalized gradient approximation of the Perdew–Burke–Ernzerhof (GGA-PBE) functional[56] as the exchange-correlation functional. We selected the projector augmented wave (PAW) method[57] to describe the core and valence electrons as well as the conjugate gradient scheme, as implemented in the Vienna ab initio simulation package (VASP)[58]. A plane-wave basis set up to a cutoff energy of 700 eV and a $10 \times 10 \times 4$, $12 \times 12 \times 4$, and $12 \times 12 \times 10$ *k*-point meshes generated by the Monkhorst–Pack (MP) method[59] were used for the $P6_3cm$ structure, the *R3c* structure, and the $P6_3/mcm$ structure, respectively. The pseudocore radii of Li, Mo, and H account for 1.7, 2.50, and 0.80 Bohrs, respectively, which are small enough to ensure that no overlap of spheres will occur under applied pressure. The zero-point energy of the nuclei (ZPE) is estimated within the harmonic approximation, which was included in the enthalpies as a function of the pressure. All values of enthalpy of all structures obtained were fitted by a Birch-Murnaghan equation of state (EOS). The dynamic stable structures were calculated by using the *ab initio* lattice dynamics with the supercell approach, as implemented in the VASP code together with the PHONOPY package[60].The plane-wave energy cutoff of 60 Ry was selected as well as a $12 \times 12 \times 10$ *k*-point mesh was used for the $P6_3/mcm$ structure. Based on the linear response theory[61], the GGA+*U* was selected as a means to perform the Hubbard *U* calculation which is implemented in Quantum Espresso (QE) package[62]. The effective interaction parameters of which were tested to be $U_{\text{eff}} = U - J = 1.2$ eV. The projected crystal orbital Hamilton population[63] (pCOHP) was used to describe the chemical bonding of the $P6_3/mcm$ structure, as implemented in LOBSTER code[64].

Received: 15 April 2020; Accepted: 1 February 2021
Published online: 18 February 2021

References

1. Lebègue, S., Alouani, M., Arnaud, B. & Pickett, W. E. Pressure-induced simultaneous metal-insulator and structural-phase transitions in LiH: a quasiparticle study. *Europhys. Lett.* **63**, 562–568 (2003).
2. Zhang, S. *et al.* Nonmetallic FeH_6 under high pressure. *J. Phys. Chem. C* **122**, 12022–12028 (2018).
3. Batalović, K., Radaković, J., Belošević-Čavor, J. & Koteski, V. Transition metal doping of Mg_2FeH_6 - a DFT insight into synthesis and electronic structure. *Phys. Chem. Chem. Phys.* **16**, 12356–12361 (2014).
4. Liu, Y. *et al.* Stability and properties of the Ru-H system at high pressure. *Phys. Chem. Chem. Phys.* **18**, 1516–1520 (2016).
5. Muramatsu, T. *et al.* Metallization and superconductivity in the hydrogen-rich ionic salt $BaReH_9$. *J. Phys. Chem. C* **119**, 18007–18013 (2015).
6. Shao, Z. *et al.* Unique phase diagram and superconductivity of calcium hydrides at high pressures. *Inorg. Chem.* **58**, 2558–2564 (2019).
7. Pluengphon, P., Bovornratanaraks, T., Tsuppayakorn-aek, P., Pinsook, U. & Inceesungvorn, B. High-pressure phases induce H-vacancy diffusion kinetics in tm-doped MgH_2: Ab initio study for hydrogen storage improvement. *Int. J. Hydrogen Energy* **44**, 21948–21954 (2019).
8. Pluengphon, P., Tsuppayakorn-aek, P., Inceesungvorn, B. & Bovornratanaraks, T. Pressure-induced structural stability of alkali trihydrides and H_2-desorption occurrence: Ab initio study for hydrogen storage improvement. *International Journal of Hydrogen Energy* (2020).
9. Salke, N. P. *et al.* Synthesis of clathrate cerium superhydride CeH_9 at 80–100 GPa with atomic hydrogen sublattice. *Nat. Commun.* **10**, 4453 (2019).
10. Somayazulu, M. *et al.* Evidence for superconductivity above 260 K in lanthanum superhydride at megabar pressures. *Phys. Rev. Lett.* **122**, 027001 (2019).
11. Wang, C., Yi, S. & Cho, J.-H. Pressure dependence of the superconducting transition temperature of compressed LaH_{10}. *Phys. Rev. B* **100**, 060502 (2019).
12. Otto, H. H. Super-hydrides of lanthanum and yttrium: On optimal conditions for achieving near room temperature superconductivity. *World J. Condens. Matter Phys.* **9**, 22–36 (2019).
13. Quan, Y. & Van Pickett, W. E. hove singularities and spectral smearing in high-temperature superconducting H_3S. *Phys. Rev. B* **93**, 104526 (2016).
14. Heil, C., di Cataldo, S., Bachelet, G. B. & Boeri, L. Superconductivity in sodalite-like yttrium hydride clathrates. *Phys. Rev. B* **99**, 220502 (2019).
15. Liang, X. *et al.* First-principles study of crystal structures and superconductivity of ternary YSH_6 and $LASH_6$ at high pressures. *Phys. Rev. B* **100**, 184502 (2019).
16. Li, X. *et al.* Polyhydride CeH_9 with an atomic-like hydrogen clathrate structure. *Nat. Commun.* **10**, 3461 (2019).
17. Drozdov, A. P. *et al.* Superconductivity at 250 K in lanthanum hydride under high pressures. *Nature* **569**, 528–531 (2019).
18. Sukmas, W., Tsuppayakorn-aek, P., Pinsook, U. & Bovornratanaraks, T. Near-room-temperature superconductivity of Mg/Ca substituted metal hexahydride under pressure. *J. Alloys Compd.* **849**, 156434 (2020).
19. Tsuppayakorn-aek, P., Pinsook, U., Luo, W., Ahuja, R. & Bovornratanaraks, T. Superconductivity of superhydride CeH_{10} under high pressure. *Mater. Res. Express* **7**, 086001 (2020).
20. Meng, D. *et al.* Superconductivity of the hydrogen-rich metal hydride Li_5MoH_{11} under high pressure. *Phys. Rev. B* **99**, 024508 (2019).
21. Takagi, S. *et al.* Formation of novel transition metal hydride complexes with ninefold hydrogen coordination. *Sci. Rep.* **7**, 44253 (2017).
22. Sit, P. H. L., Car, R., Cohen, M. H. & Selloni, A. Simple, unambiguous theoretical approach to oxidation state determination via first-principles calculations. *Inorg. Chem.* **50**, 10259–10267 (2011).
23. Lutfalla, S., Shapovalov, V. & Bell, A. T. Calibration of the DFT/GGA+U method for determination of reduction energies for transition and rare earth metal oxides of Ti, V, Mo, and Ce. *J. Chem. Theory Comput.* **7**, 2218–2223 (2011).
24. Zhou, F. *et al.* Pnma metal hydride system LiBH: a superior topological semimetal with the coexistence of twofold and quadruple degenerate topological nodal lines. *J. Phys.: Condens. Matter* **32**, 365502 (2020).
25. Yang, T., Cheng, Z., Surucu, G. & Wang, X. Coexistence of parabolic and linear band crossings and electron-doped spin-gapless properties in rhombohedral type $YbBO_3$. *J. Alloys Compd.* **823**, 153835 (2020).
26. Wang, X. *et al.* Rich topological nodal line bulk states together with drum-head-like surface states in NaAlGe with anti-PbFCl type structure. *J. Adv. Res.* **23**, 95–100 (2020).
27. Wang, X. *et al.* Novel topological nodal lines and exotic drum-head-like surface states in synthesized CsCl-type binary alloy tios. *J. Adv. Res.* **22**, 137–144 (2020).
28. Tsuppayakorn-aek, P. *et al.* Bain deformation mechanism and Lifshitz transition in magnesium under high pressure. *Phys. Status Solidi B* 2000279 (2020).
29. Xu, C. Q. *et al.* Topological phase transition under pressure in the topological nodal-line superconductor $PbTaSe_2$. *Phys. Rev. B* **96**, 064528 (2017).
30. Zhang, Y. *et al.* Pressure effect on kohn anomaly and electronic topological transition in single-crystal tantalum. *Phys. Rev. B* **100**, 075145 (2019).
31. Bjornsson, R. *et al.* Identification of a spin-coupled Mo(iii) in the nitrogenase iron-molybdenum cofactor. *Chem. Sci.* **5**, 3096–3103 (2014).
32. Tian, M.-F., Deng, X., Fang, Z. & Dai, X. Intermediate-pressure phases of cerium studied by an LDA + Gutzwiller method. *Phys. Rev. B* **84**, 205124 (2011).
33. Zhou, L. *et al.* Structural stability and thermodynamics of CrN magnetic phases from ab initio calculations and experiment. *Phys. Rev. B* **90**, 184102 (2014).
34. Hou, L., Li, W.-D., Wang, F., Eriksson, O. & Wang, B.-T. Structural, electronic, and thermodynamic properties of curium dioxide: Density functional theory calculations. *Phys. Rev. B* **96**, 235137 (2017).
35. Isaacs, E. B. & Marianetti, C. A. Compositional phase stability of strongly correlated electron materials within DFT+U. *Phys. Rev. B* **95**, 045141 (2017).
36. Abe, K. Ab initio study of metallic aluminum hydrides at high pressures. *Phys. Rev. B* **100**, 174105 (2019).
37. Ye, X., Zarifi, N., Zurek, E., Hoffmann, R. & Ashcroft, N. W. High hydrides of scandium under pressure: Potential superconductors. *J. Phys. Chem. C* **122**, 6298–6309 (2018).
38. Zhang, J. *et al.* High-temperature superconductivity in the Ti-H system at high pressures. *Phys. Rev. B* **101**, 134108 (2020).
39. Bianco, R., Errea, I., Calandra, M. & Mauri, F. High-pressure phase diagram of hydrogen and deuterium sulfides from first principles: Structural and vibrational properties including quantum and anharmonic effects. *Phys. Rev. B* **97**, 214101 (2018).

40. Olea-Amezcua, M. A., De la Peña Seaman, O. & Heid, R. Superconductivity by doping in alkali-metal hydrides without applied pressure: An ab initio study. *Phys. Rev. B* **99**, 214504 (2019).
41. Pereira, A. L. J. *et al.* Isostructural second-order phase transition of β-Bi_2O_3 at high pressures: An experimental and theoretical study. *J. Phys. Chem. C* **118**, 23189–23201 (2014).
42. Mack, S. A., Griffin, S. M. & Neaton, J. B. Emergence of topological electronic phases in elemental lithium under pressure. *Proc. Natl. Acad. Sci.* **116**, 9197 (2019).
43. Elatresh, S. F. *et al.* High-pressure lithium as an elemental topological semimetal. *Phys. Rev. Mater.* **3**, 044203 (2019).
44. Lifshitz, I. *et al.* Anomalies of electron characteristics of a metal in the high pressure region. *Sov. Phys. JETP* **11**, 1130–1135 (1960).
45. Kubo, K. Ferromagnetism and Fermi surface transition in the periodic Anderson model: Second-order phase transition without symmetry breaking. *Phys. Rev. B* **87**, 195127 (2013).
46. Becke, A. D. & Edgecombe, K. E. A simple measure of electron localization in atomic and molecular systems. *J. Chem. Phys.* **92**, 5397–5403 (1990).
47. Tsuppayakorn-aek, P., Luo, W., Watcharatharapong, T., Ahuja, R. & Bovornratanaraks, T. Structural prediction of host-guest structure in lithium at high pressure. *Sci. Rep.* **8**, 5278 (2018).
48. Tsuppayakorn-aek, P. *et al.* The ideal commensurate value of Sc and the superconducting phase under high pressure. *J. Appl. Phys.* **124**, 225901 (2018).
49. Bovornratanaraks, T., Tsuppayakorn-aek, P., Luo, W. & Ahuja, R. Ground-state structure of semiconducting and superconducting phases in xenon carbides at high pressure. *Sci. Rep.* **9**, 2459 (2019).
50. Tsuppayakorn-Aek, P. *et al.* Route to high-T_c superconductivity of BC_7 via strong bonding of boron-carbon compound at high pressure. *Sci. Rep.* **10**, 1–8 (2020).
51. Zhao, Z. *et al.* Potentially superhard hcp CrN_2 compound studied at high pressure. *Phys. Rev. B* **93**, 214104 (2016).
52. Peng, F. *et al.* Hydrogen clathrate structures in rare earth hydrides at high pressures: Possible route to room-temperature superconductivity. *Phys. Rev. Lett.* **119**, 107001 (2017).
53. Kotmool, K. *et al.* Structural phase transitions, electronic properties, and hardness of RuB_4 under high pressure in comparison with FeB_4 and OsB_4. *J. Phy. Chem. C* (2020).
54. Dubois, S. M. M., Zanolli, Z., Declerck, X. & Charlier, J. C. Electronic properties and quantum transport in graphene-based nanostructures. *Eur. Phys. J. B* **72**, 1–24 (2009).
55. Oganov, A. R. & Glass, C. W. Crystal structure prediction using ab initio evolutionary techniques: Principles and applications. *J. Chem. Phys.* **124**, 244704 (2006).
56. Perdew, J. P., Burke, K. & Ernzerhof, M. Generalized gradient approximation made simple. *Phys. Rev. Lett.* **77**, 3865–3868 (1996).
57. Blöchl, P. E. Projector augmented-wave method. *Phys. Rev. B* **50**, 17953–17979 (1994).
58. Kresse, G. & Furthmüller, J. Efficient iterative schemes for ab initio total-energy calculations using a plane-wave basis set. *Phys. Rev. B* **54**, 11169–11186 (1996).
59. Monkhorst, H. J. & Pack, J. D. Special points for brillouin-zone integrations. *Phys. Rev. B* **13**, 5188–5192 (1976).
60. Togo, A. & Tanaka, I. First principles phonon calculations in materials science. *Scr. Mater.* **108**, 1–5 (2015).
61. Cococcioni, M. & de Gironcoli, S. Linear response approach to the calculation of the effective interaction parameters in the LDA + U method. *Phys. Rev. B* **71**, 035105 (2005).
62. Giannozzi, P. *et al.* Quantum espresso: a modular and open-source software project for quantum simulations of materials. *J. Phys.: Condens. Matter* **21**, 395502 (2009).
63. Deringer, V. L., Tchougréeff, A. L. & Dronskowski, R. Crystal orbital hamilton population (COHP) analysis as projected from plane-wave basis sets. *J. Phys. Chem. A* **115**, 5461–5466 (2011).
64. Maintz, S., Deringer, V. L., Tchougréeff, A. L. & Dronskowski, R. Lobster: A tool to extract chemical bonding from plane-wave based DFT. *J. Comput. Chem.* **37**, 1030–1035 (2016).
65. Momma, K. & Izumi, F. Vesta: a three-dimensional visualization system for electronic and structural analysis. *J. Appl. Crystallogr.* **41**, 653–658 (2008).
66. Kokalj, A. Xcrysden—a new program for displaying crystalline structures and electron densities. *J. Mol. Graph. Model.* **17**, 176–179 (1999).

Acknowledgements

We are deeply grateful for the kindness of Dezhong Meng, Shigeyuki Takagi, and Shin-ichi Orimo for suggestions. We gratefully acknowledge the NSC (National Supercomputer Centre, Linköping, Sweden) in Sweden for providing computing time. This research project is supported by Second Century Fund (C2F), Chulalongkorn University. This project is funded by National Research Council of Thailand (NRCT): (NRCT5-RSA63001-04) and Chulalongkorn University, Grant for Research. R.A. and W.L. thank the Swedish Research Council and Swedish Research Links for financial support.

Author contributions

Author contributions: P.T. and T.B. designed the research; P.T. and T.B performed the research; P.T. and T.B. analysed the data; and P.T., R.A., W.L, and T.B. wrote the paper; W.S. and T.B corrected the paper.

Competing interests

The authors declare no competing interests.

Additional information

Correspondence and requests for materials should be addressed to T.B.

Reprints and permissions information is available at www.nature.com/reprints.

Publisher's note Springer Nature remains neutral with regard to jurisdictional claims in published maps and institutional affiliations.